




Review

# Area-Detector Computed Tomography for Pulmonary Functional Imaging

Yoshiharu Ohno <sup>1,2,\*</sup>, Yoshiyuki Ozawa <sup>3</sup>, Hiroyuki Nagata <sup>2</sup>, Shuji Bando <sup>3</sup>, Shang Cong <sup>3</sup>, Tomoki Takahashi <sup>3</sup>, Yuka Oshima <sup>3</sup>, Nayu Hamabuchi <sup>3</sup>, Takahiro Matsuyama <sup>3</sup>, Takahiro Ueda <sup>3</sup>, Takeshi Yoshikawa <sup>4</sup>, Daisuke Takenaka <sup>4</sup> and Hiroshi Toyama <sup>3</sup>

<sup>1</sup> Department of Diagnostic Radiology, Fujita Health University School of Medicine, Toyoake 470-1192, Aichi, Japan

<sup>2</sup> Joint Research Laboratory of Advanced Medical Imaging, Fujita Health University School of Medicine, Toyoake 470-1192, Aichi, Japan; nagata\_zaiken@yahoo.co.jp

<sup>3</sup> Department of Radiology, Fujita Health University School of Medicine, Toyoake 470-1192, Aichi, Japan; yoshiyuki.ozawa@fujita-hu.ac.jp (Yoshiyuki Ozawa)

<sup>4</sup> Department of Diagnostic Radiology, Hyogo Cancer Center, Akashi 673-0021, Hyogo, Japan

\* Correspondence: yohnofujita-hu.ac.jp; Tel.: +81-562-93-9259; Fax: +81-562-95-2253

**Abstract:** An area-detector CT (ADCT) has a 320-detector row and can obtain isotropic volume data without helical scanning within an area of nearly 160 mm. The actual-perfusion CT data within this area can, thus, be obtained by means of continuous dynamic scanning for the qualitative or quantitative evaluation of regional perfusion within nodules, lymph nodes, or tumors. Moreover, this system can obtain CT data with not only helical but also step-and-shoot or wide-volume scanning for body CT imaging. ADCT also has the potential to use dual-energy CT and subtraction CT to enable contrast-enhanced visualization by means of not only iodine but also xenon or krypton for functional evaluations. Therefore, systems using ADCT may be able to function as a pulmonary functional imaging tool. This review is intended to help the reader understand, with study results published during the last a few decades, the basic or clinical evidence about (1) newly applied reconstruction methods for radiation dose reduction for functional ADCT, (2) morphology-based pulmonary functional imaging, (3) pulmonary perfusion evaluation, (4) ventilation assessment, and (5) biomechanical evaluation.

**Keywords:** lung; multidetector computed tomography; area-detector CT; pulmonary function; radiation dose



**Citation:** Ohno, Y.; Ozawa, Y.; Nagata, H.; Bando, S.; Cong, S.; Takahashi, T.; Oshima, Y.; Hamabuchi, N.; Matsuyama, T.; Ueda, T.; et al. Area-Detector Computed Tomography for Pulmonary Functional Imaging. *Diagnostics* **2023**, *13*, 2518. <https://doi.org/10.3390/diagnostics13152518>

Academic Editor: Chiara Martini

Received: 5 June 2023

Revised: 22 July 2023

Accepted: 25 July 2023

Published: 28 July 2023



**Copyright:** © 2023 by the authors. Licensee MDPI, Basel, Switzerland. This article is an open access article distributed under the terms and conditions of the Creative Commons Attribution (CC BY) license (<https://creativecommons.org/licenses/by/4.0/>).

## 1. Introduction

Since the clinical installation of a multidetector row CT (MDCT) in 1999 [1], detector rows have been increased from 4 to 64 by every vendor almost every 2 years to result in area-detector CT (ADCT) systems with 256- or 320-detector rows, which are now widely used in routine clinical practice worldwide since their introduction in 2007. With ADCT, isotropic volume data for the entire brain, heart, or some other organs, as well as for entire tumors, can be acquired almost immediately within an area of nearly 160 mm without helical scanning. Whole-organ-perfusion CT data can, thus, be obtained by means of continuous dynamic scanning, allowing for the qualitative and/or quantitative evaluation of the perfusion of some organs as well as of pulmonary nodules, lymph nodes, or lung cancer for a variety of clinical aims [2–23]. Moreover, the system can obtain CT data with both helical scanning and step-and-shoot or wide-volume scanning for body CT imaging. In addition, ADCT has the potential to perform dual-energy CT and subtraction CT, which is another promising technique for enhancing the visualization of contrast enhancement by using iodine contrast media as well as xenon or krypton for functional evaluations. Therefore, ADCT systems are now being used for not only morphological examinations

but also functional assessments for a variety of clinical purposes including pulmonary functional imaging.

This review will focus on (1) new reconstruction methods being used for radiation dose reduction for functional ADCT, (2) morphology-based pulmonary functional imaging, (3) pulmonary perfusion evaluation, (4) ventilation assessment, and (5) biomechanical evaluation using ADCT because these items have proven to yield fruitful results during the last few decades.

## 2. New Reconstruction Methods Used for Radiation Dose Reduction for Functional ADCT

For the last decade or so, dose reduction strategies have been relying on a variety of techniques for data acquisition, such as tube current or tube voltage reduction, increased helical pitch, scan length optimization, and the utilization of automatic exposure control (AEC) [24–30]. In general, the image noise is inversely proportional to the square root of the radiation dose, so reduced-dose CT images have a higher noise level than standard-dose images, and care must be exercised to ensure that the former remain suitable for diagnosis. To overcome the increase in image noise on reduced-dose CT images, various imaging filters, reconstruction algorithms, and kernels have been developed. Since the early 2010s, most CT vendors have clinically installed hybrid-type or model-based iterative reconstruction (IR) algorithms for use in routine clinical practice, and many practitioners have found them useful for cardiothoracic imaging. For hybrid-type IR, hybrid algorithms combine both analytical and iterative methods so that the initial image can be generated by means of analytical methods, followed by the use of iterative methods to reduce noise in the image domain. However, iterative algorithms can also be directly employed for the reconstruction process. The term hybrid IR usually refers to algorithms that mainly reduce image noise through cyclic image processing [27–30], while the term model-based IR usually refers to algorithms that employ models of the acquisition process, image statistics, and system geometry. Although the clinical performance of IR algorithms is not necessarily related to the complexity of the method [31], the reconstruction of hybrid-type IR algorithms is generally faster than that of model-based IR algorithms, and it is more easily applied in routine clinical practice. In 2019, deep learning reconstruction (DLR) was introduced and clinically installed and tested by a few vendors [32–37]. These methods can be grouped into two major categories, indirect and direct DLR frameworks [37]. For indirect DLR frameworks, either filtered back projection (FBP) or IR is used. The three types of indirect frameworks, sinogram-based, image-based, and hybrid, are differentiated based on when the deep learning network is deployed. Sinogram-based frameworks focus on sinogram optimization, and the network is deployed before the sinogram is treated with FBP or IR. For image-based frameworks, the network optimizes the image after initial reconstruction with FBP or IR, while hybrid frameworks combine the sinogram with image optimization [37]. Direct DLR algorithms reconstruct the sinogram directly into an image without the use of FBP or IR. This can reduce artifacts introduced by FBP or IR, but this is only possible if the ground truth images used for model training do not contain FBP- or IR-related artifacts [37]. The currently used hybrid-type and model-based IR and DLR methods from major vendors are shown in Table 1.

During the last few decades, ADCT has been used for the aforementioned reconstruction methods to reduce the radiation dose for various clinical purposes, and the results have been published. One study reported that the image quality obtained with tube currents of 100 mA and 50 mA and an FBP algorithm was significantly lower than that for both protocols using AIDR 3D, one of the hybrid-type IR methods, for image reconstruction [27]. Moreover, all inter-method agreements for bronchiectasis, emphysema, ground-glass opacity, honeycomb pattern, interlobar septal thickening, nodules, and reticular opacity ranged from moderate to substantial or almost perfect. Furthermore, all agreements for the mediastinal and pleural findings among reduced-dose CTs using AIDR 3D algorithms and standard-dose CT using an FBP algorithm were almost perfect [27]. In addition, the Area-

Detector Computed Tomography for the Investigation of Thoracic Diseases (ACTIve) study group conducted a multicenter study to assess the image quality and radiation dose reduction in the case of chest CT using AIDR 3D, but their study used standard-dose CT with a tube current of 240 mA and reduced-dose CTs with tube currents of 120 mA and 60 mA [38]. The same group also assessed the utility of the AIDR 3D algorithm for lung nodule detection on reduced-dose CT [39]. No significant differences in solid lung nodule detection were found between reduced-dose CT protocols using tube currents of 120 mA and 20 mA. Moreover, a comparison of ground-glass nodule (GGN) detection capability showed that the capability of the two protocols for detecting GGNs with a diameter equal to or more than 8 mm was not significantly different [39]. Another study found that further radiation dose reduction without significant degradation of subsolid nodule detection was obtained with the same hybrid-type IR method [40]. As a result of these published findings, AIDR 3D for ADCT is currently used in routine clinical practice.

**Table 1.** Hybrid-type iterative reconstruction, model-based iterative reconstruction, and deep learning reconstruction methods provided by major CT vendors.

Vendor	Reconstruction Methods		
	Hybrid-Type IR	Model-Based IR	DLR
Canon Medical Systems	Adaptive Iterative Dose Reduction 3D (AIDR 3D)	Forward Projected Model-Based Iterative Reconstruction Solution (FIRST)	Advanced intelligent Clear-IQ Engine (AiCE)
GE Healthcare	Adaptive Statistical Iterative Reconstruction (ASiR)	Veo	TrueFidelity
Philips Healthcare	4th-Generation Iterative Reconstruction (iDose <sup>4</sup> )	Iterative Model Reconstruction (IMR)	Precise Image
Siemens Healthineers	Iterative Reconstruction in Image Space (IRIS)		
	Sinogram Affirmed Iterative Reconstruction (SAFIRE)	N/A	N/A
	Advanced Modeled Iterative Reconstruction (ADMIRE)		

IR: iterative reconstruction, DLR: deep learning reconstruction.

For pulmonary functional imaging, the Quantitative Imaging Biomarkers Alliance (QIBA) of the Radiological Society of North America (RSNA) has been developing QIBA profiles based on in vitro study findings for lung density since 2007 to standardize the CT protocol for 64-detector-row CTs from major vendors [41]. In collaboration with the QIBA, the Japan Quantitative Imaging Biomarker Alliance (J-QIBA) of the Japan Radiological Society has been testing and has confirmed the capabilities of each of the state-of-the-art reconstruction techniques, such as hybrid-type IR, model-based IR, or DLR for the same settings, as well as airway dimension evaluation for not only ADCT but also high-definition CT (HDCT) or ultra-high-resolution CT (UHR-CT) [42,43]. These studies proved that all state-of-the-art reconstruction methods have the potential ability to reduce the radiation dose of chest CT while maintaining the requirements from the QIBA profile for QIBA-recommended phantom studies [42,43]. Therefore, by combining state-of-the-art reconstruction methods with ADCT, pulmonary functional CT can be assessed in routine clinical practice in terms of not only morphological but also functional information by using various procedures detailed in the sections that follow.

### 3. Morphology-Based Pulmonary Functional Imaging

Like other MDCTs, morphology-based pulmonary functional ADCT has been used for the quantitative assessment of chronic obstructive pulmonary disease (COPD), interstitial lung disease (ILD), or other diseases by using not only standard- but also reduced-dose protocols [27,31,38–47].

For COPD assessments, CT can be used to assess morphological and functional changes related to COPD [48–60]. During the last few decades, many commercially available and proprietary software products as well as various visual scoring systems have been used for the CT-based assessment of COPD, with two major approaches reported in the literature for quantitative CT assessment of COPD [48–60]. One is the determination of the percentage of low attenuation area (%LAA) in the lung, which indicates emphysema changes, and the other is the determination of the wall area ratio (WA%) of the bronchi, which indicates bronchial lumen narrowing and bronchial wall thickening [48–60]. In the past literature [48–60], it has been suggested that the %LAA has a good correlation with  $FEV_1/FVC$ ,  $\%FEV_1$ ,  $\%DL_{CO}$ , or  $DL_{CO}/V_A$  and that the WA% also has a good correlation with  $FEV_1/FVC$  and  $\%FEV_1$ . Therefore, it is suggested that these imaging parameters are useful as quantitative imaging biomarkers for COPD [48–60]. In addition, three-dimensional (3D) airway luminal volumetry has been introduced as another quantitative method for evaluating the airways of COPD patients [58,59]. Taking the findings provided by these quantitative CT assessments of COPD and the need for radiation dose reduction strategies into consideration [42–46,58–60], the application of IR algorithms has been considered an important issue for an accurate quantitative CT evaluation of COPD. One study demonstrated that agreement for the %LAA between standard-dose CT obtained at 300 mA and reduced-dose CT at 50 mA tended to improve when using AIDR 3D rather than conventionally applied FBP [44] (Figure 1).

Moreover, the ACTive study group applied the same hybrid-type IR algorithm and obtained similar results for standard-dose CT at 240 mA and reduced-dose CTs at 120 mA and 60 mA [60]. Thus, the use of a hybrid-type IR resulted in greater consistency of emphysema quantifications performed on reduced-dose and ultra-low-dose CTs than on standard-dose CT images. Although the %LAA and the WA% have been recommended as the two main quantitative parameters for COPD assessment [41–60], 3D airway luminal volumetry has also been introduced as another method for quantitative ADCT evaluation of airflow limitation in COPD [58,59]. Koyama et al. assessed the utility of a hybrid-type IR algorithm for quantitative bronchial assessment on reduced-dose CT for patients with and without COPD and provided evidence of a significant correlation of WA% and the airway luminal volume percentage from the main bronchus to the peripheral bronchi (LV%) between standard- and reduced-dose CT [58]. Moreover, LV% agreement between standard-dose and reduced-dose CTs can improve AIDR 3D in comparison with FBP [59]. Therefore, AIDR 3D can be recommended for quantitative COPD evaluation on ADCT in routine clinical practice.

Few studies have been published on radiation dose reduction for the use of ADCT for the quantitative assessment of morphological evaluation of ILD. However, the utility of commercial or proprietary artificial intelligences (AIs) using machine-learning methods by Canon Medical Systems has been evaluated for the management of various lung diseases, such as ILD, or the evaluation of therapeutic treatments for coronavirus disease 2019 (COVID-19) pneumonia, which is caused by severe acute respiratory syndrome coronavirus 2 (SARS-CoV-2) [61–63] (Figure 2).

These studies were the first to demonstrate the potential of AI in the evaluation of disease severity and therapeutic effect or of functional changes due to treatment with an accuracy similar to that attained by board-certified radiologists [61–63]. Although further investigations are warranted, the evaluation of ADCT by AI has opened new areas for the application of pulmonary functional ADCT in not only ILD but also other diseases.

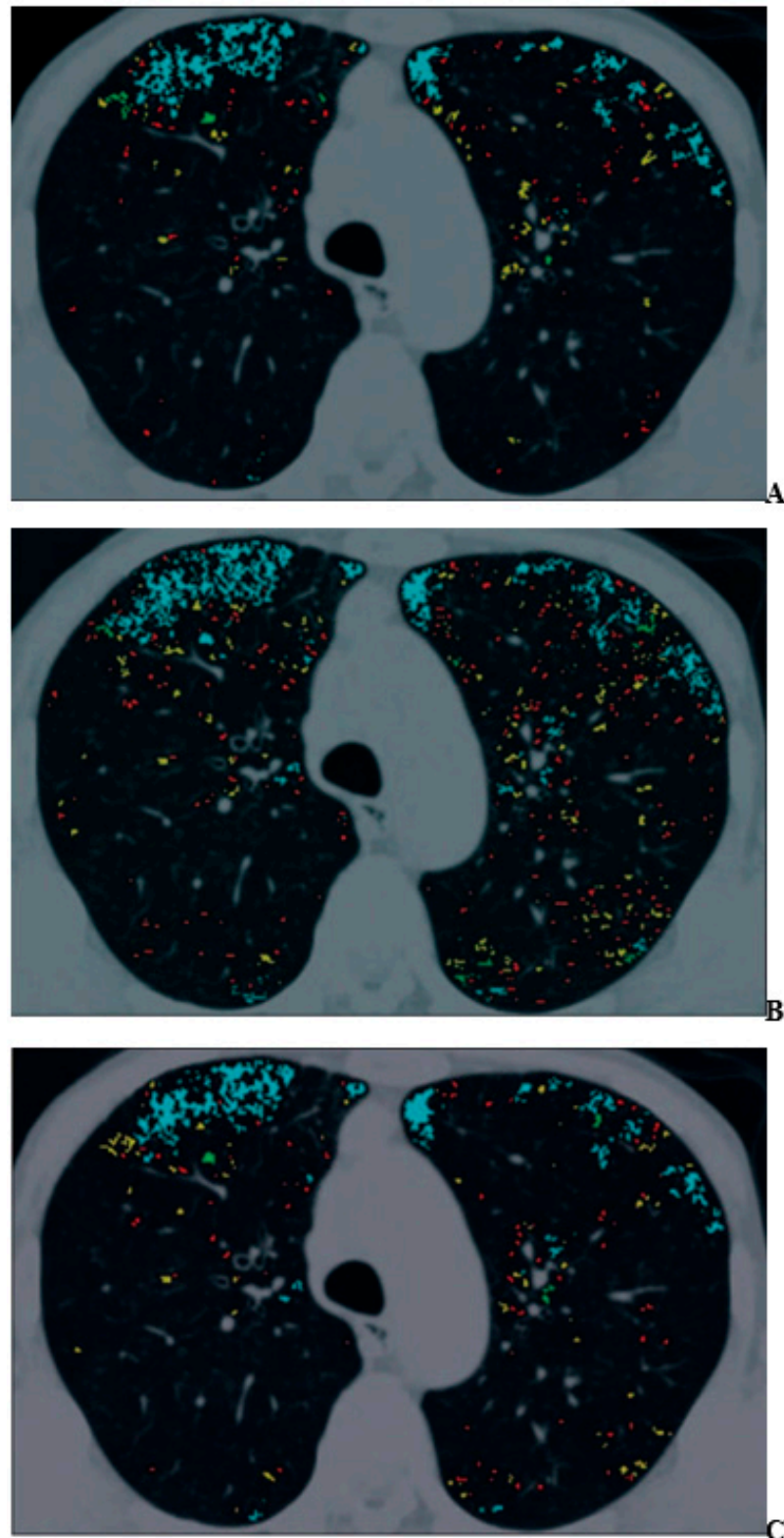


**Figure 1.** A 70-year-old man with mild pulmonary emphysema (permission from reference [44]). (A–C) Images show low-attenuation lung regions with standard-dose CT (A), low-dose CT without adaptive iterative dose reduction using 3D processing (B), and low-dose CT with adaptive iterative dose reduction using 3D processing (C). Color coding of low-attenuation lung regions is as follows: class 1, red; class 2, yellow; class 3, green; and class 4, cyan.

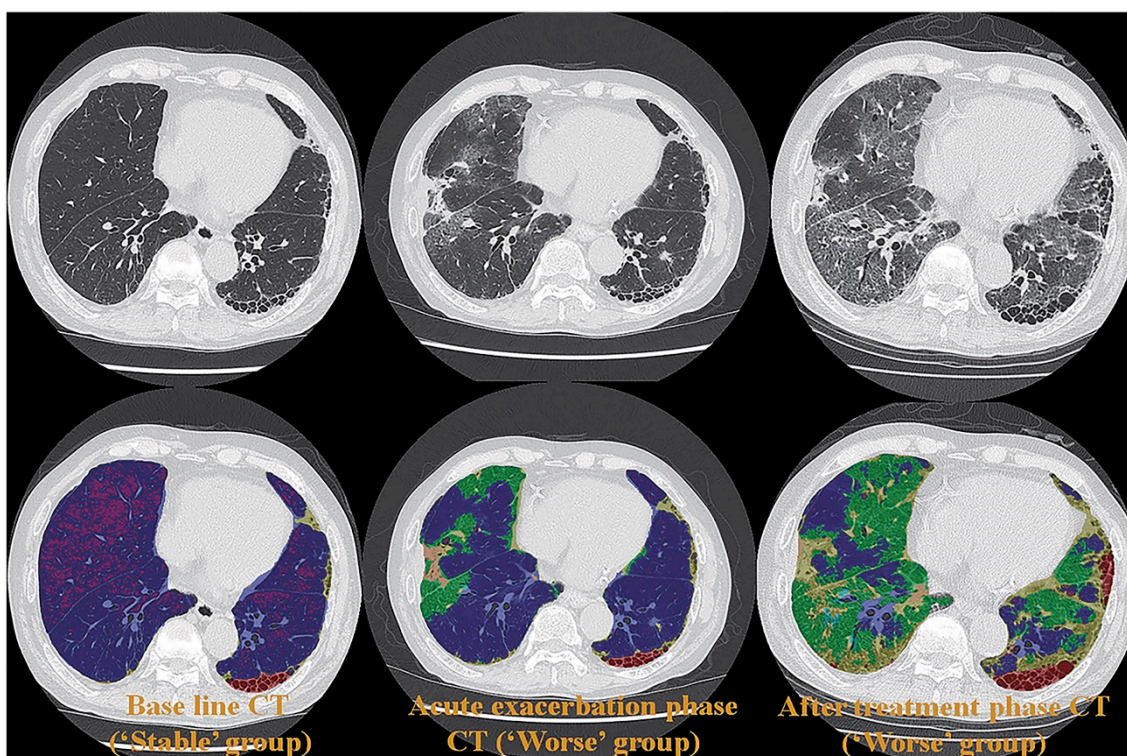


**Figure 2.** A 65-year-old female patient with progressive scleroderma (top row, L to R: thin-section CT scans at baseline, acute exacerbation phase, and after-treatment phase; bottom row, L to R: CT texture analysis by means of machine-learning-based software at baseline and the same two phases as for the top row) (permission from reference [63]). On machine-learning software, normal lung, consolidation, emphysema, GGO, honeycombing and reticulation are expressed as blue, beige, purple, green, red and green. A comparison of CT scans obtained at baseline (i.e., “Stable” group) and at the acute exacerbation phase (i.e., “Worse” group) shows an increase in the GGO and the consolidation area and a decrease in the normal lung area.  $\Delta\%$  normal lung,  $\Delta\%$  GGO, and  $\Delta\%$  consolidation were  $-16.9\%$ ,  $13.2\%$ , and  $2.5\%$ , respectively, while  $\Delta$  disease severity score was 6. A comparison of CT scans obtained at the acute exacerbation phase (i.e., “Worse” group) and the after-treatment phase (i.e., “Worse” group) shows an increase in the GGO, reticulation, and honeycomb area and a decrease in the normal lung area.  $\Delta\%$  normal lung,  $\Delta\%$  GGO,  $\Delta\%$  reticulation, and  $\Delta\%$  honeycomb were  $-19.5\%$ ,  $14.9\%$ ,  $4.2\%$ , and  $0.2\%$ , while  $\Delta$  disease severity score was 15. CT, computed tomography; GGO, ground-glass opacity.

#### 4. Pulmonary Perfusion Evaluation

Starting in the late 1960s, pulmonary perfusion was mainly assessed by means of nuclear medicine studies such as perfusion scanning, perfusion single-photon emission tomography (SPECT), or SPECT fused with CT (SPECT/CT). Since the late 1990s, pulmonary perfusion has also been academically or clinically assessed by using non-contrast-enhanced (non-CE) or contrast-enhanced (CE) perfusion MR imaging (non-CE- or CE-MRI) with a variety of techniques [64–70]. However, the application of each perfusion MR imaging procedure remains limited because of several technical issues such as pulse sequence design and optimization, certain procedures including contrast media concentration differentiation for quantitative or qualitative evaluation, somewhat lower temporal resolution than CT, and image analysis software for different clinical purposes [64–70]. As a result, pulmonary perfusion evaluation on CT has been performed since 2008 by means of three different methods: (i) dual-energy CT (DECT), (ii) subtraction CT (subtracting non-CE- from CE-CT images), and (iii) dynamic first-pass CE-perfusion CT.

#### 4.1. Dual-Energy CT with ADCT System

Since the dual-source CT was installed for clinical use in 2008, DECT has been tested to assess its clinical utility for not only pulmonary vascular diseases but also other thoracic diseases [67,68,71–77]. This was followed, until recently, by the installation for testing and clinical use of rapid tube voltage (kVp) switching, dual-layer, or split-beam techniques for DECT. Table 2 shows a summary of the state-of-the-art DECT techniques provided by major vendors for routine clinical practice.

**Table 2.** Dual-energy CT techniques currently available from major vendors.

Multienergy CT Technique	Dual Source	Split Beam	Rapid kVp Switching		Dual-Layer Detector
CT vendors	Siemens Healthineers	GE Healthcare	Canon Medical Systems		Philips Healthcare
Number of X-ray tubes	2	1	1	1	1
Scan time (sec/rotation)	0.25	0.28	0.28	0.275	0.27
FOV	Small in one X-ray tube	Full	Full	Full	Full
Z-axis coverage/rotation (mm/rot)	57.6–80	40	80	40–160	40–80
Automatic exposure control	Yes	No	Yes	Yes	Yes
Cross scattering	Yes	No	No	No	No
Filter	Yes	No	No	No	No
Registration	Slight temporal offset	Poor	Good	Good	Good
Spectral reconstruction method	Image	Projection and image	Projection and image	Projection and image	Projection and image
Tube current optimization for different energy bin	Yes	No	No	No	No
Spectral separation	Good	Limited	Good	Good	Limited

Although it has been suggested that DECT, similar to perfusion scan or SPECT, is useful for the evaluation of pulmonary perfusion in various pulmonary diseases [67,68,71–77], few major studies have been conducted on DECT-based assessment for the ADCT system. New clinical studies are, therefore, warranted in the near future to evaluate the clinical relevance of DECT for ADCT system for patients with various pulmonary diseases.

#### 4.2. Subtraction ADCT

In contrast to DECT for the ADCT system, pulmonary perfusion evaluation for ADCT has been made possible by use of the subtraction technique with the appropriate software [78–84]. An in vitro study demonstrated that the contrast-to-noise ratio (CNR) of subtraction ADCT was superior to that of DECT by assessment with different iodine contrast media phantoms [79,80], while another in vivo study confirmed the superior clinical potential of subtraction ADCT in comparison with that of CE-CT pulmonary angiography (CE-CTPA) or DECT [81–83]. Moreover, lung subtraction iodine mapping by subtraction ADCT was shown to perform significantly better than CE-CTPA for patients with chronic thromboembolic pulmonary hypertension (CTEPH) [82]. In addition, in comparison with perfusion SPECT as the reference standard, lung subtraction iodine mapping with CE-CTPA showed promising results, with a sensitivity of 81.3% and a specificity of 78.9%, for the assessment of pulmonary perfusion in patients with acute pulmonary thromboembolism (PE) [83]. Moreover, subtraction ADCT was quantitatively and qualitatively directly compared with DECT for the assessment of lung nodule enhancement [84]. That study demonstrated that the mean nodule enhancement for subtraction ADCT was significantly

higher than that for DECT. Lastly, the nodule enhancement on subtraction ADCT was judged more often to be “highly visible” than that on DECT by each of the observers engaged in that study. Subtraction ADCT was, therefore, considered to have better potential than DECT for iodine enhancement depiction in lung nodules [84]. Although subtraction ADCT is not as frequently used as DECT, this technique is potentially superior to DECT for the evaluation in routine clinical practice of differences in iodine contrast medium concentration through pixel-by-pixel analysis for not only thoracic but also other diseases when used with the appropriate software.

#### 4.3. Dynamic First-Pass CE-Perfusion ADCT

The use of quantitatively analyzed dynamic first-pass CE-perfusion CT by means of electron-beam CT was first reported in 2000 [85]. However, after the introduction of MDCT, the use of electron-beam CT for this type of CT examination was changed to MDCT. This was followed by reports by some investigators, published between 2000 and 2010, that quantitative assessment of tumor or nodule perfusion assessment had potential for the diagnosis of pulmonary nodules or lung cancer, as well as for therapeutic effect assessment of lung cancer patients undergoing conservative therapy [85–92]. However, the limited scan range attainable with dynamic scanning in the same table position or the variety of perfusion data obtained at different time points and positions within the scan range due to the helical scan method remained major drawbacks of this technique until 2007 [87–89]. Since then, real dynamic first-pass CE-perfusion ADCT data in the form of isotropic volume data can be obtained by means of continuous dynamic scanning, allowing for the qualitative and quantitative evaluation of the perfusion of pulmonary nodules, lymph nodes, and tumors within a 160 mm area [5,12,14–22]. As a result, ADCT systems are now being used for both morphologic examinations and functional assessments, especially real first-pass perfusion evaluation, by means of the dynamic first-pass CE-perfusion ADCT technique using the appropriate mathematical models [5,12,14–22]. Table 3 lists the major clinical evidence with regard to dynamic first-pass CE-perfusion ADCT published during the last few decades.

For the diagnosis of pulmonary nodules, the diagnostic performance of dynamic first-pass CE-perfusion ADCT was equal to or significantly better than that of FDG-PET/CT or dynamic first-pass CE-perfusion MRI with a 1.5 T or 3 T MR system [15,21,22] (Figure 3).

Moreover, the diagnostic performance of dynamic first-pass CE-perfusion ADCT for lymph node metastasis was also shown to be equal to or significantly better than that of FDG-PET/CT for non-small-cell lung cancer (NSCLC) patients [20]. In addition, the dual-input maximum slope model was found to have better potential for accurate evaluation than the single-input maximum slope or Patlak plot methods in the aforementioned settings [19]. A comparison of the capability of response evaluation criteria to differentiate solid-tumor (RECIST) responders from RECIST non-responders in NSCLC patients treated with conservative therapy showed no significant differences in the sensitivity, specificity, and accuracy of dynamic first-pass CE-perfusion ADCT, MRI analyzed with the same dual-input maximum slope model, or FDG-PET/CT [22]. Furthermore, hybrid-type IR was shown to be more effective than FBP in terms of dose reduction for dynamic first-pass CE-perfusion ADCT while maintaining image quality and reducing measurement errors [16]. Dynamic first-pass CE-perfusion ADCT with an appropriate mathematical model as well as a reconstruction method, therefore, merits use as a pulmonary functional imaging method in routine clinical practice. Furthermore, Canon Medical systems is now developing and testing an appropriate protocol and proprietary software for the analysis of whole-lung dynamic first-pass CE-perfusion ADCT data and the creation of a whole-lung perfusion parameter map for a variety of different academic and clinical purposes, which will be made available for use in the near future.



**Table 3.** Major clinical evidence for dynamic first-pass CE-perfusion ADCT.

Authors	Method	Target	Parameters	Cutoff Values (HU)	SE (%)	SP (%)	AC (%)
Ohno Y, et al. [5]	320-detector row CT	Pulmonary nodules	Perfusion (mL/100 mL/min) calculated with single-input maximum slope method	40.0	98 (42/43)	79 (26/33)	90 (68/76)
			Extraction fraction (mL/100 mL/min)	2.0	88 (38/43)	82 (27/33)	86 (65/76)
			Blood volume (mL/100 mL)	2.0	86 (37/43)	54 (18/33)	72 (55/76)
	FDG-PET/CT		SUV <sub>max</sub>	2.0	91 (39/43)	52 (17/33)	74 (56/76)
Ohno Y, et al. [12]	320-detector row CT	Pulmonary nodules	Total perfusion (mL/100 mL/min) calculated with dual-input maximum slope method	40	86.0 (49/57)	79.5 (31/39)	83.3 (80/96)
			Perfusion (mL/100 mL/min) calculated with single-input maximum slope method	20	64.9 (37/57)	69.2 (27/39)	66.7 (64/96)
			SUV <sub>max</sub>	2.5	63.2 (36/57)	56.4 (22/39)	60.4 (58/96)
Ohno Y, et al. [15]	320-detector row CT	Pulmonary nodules	Total perfusion (mL/100 mL/min) calculated with dual-input maximum slope method	29	92 (123/133)	71 (60/85)	84 (183/218)
			Nodule perfusion (mL/100 mL/min) calculated with single-input maximum slope method	10	91 (121/133)	28 (24/85)	67 (145/218)
			Maximum relative enhancement	0.13	92 (123/133)	49 (42/85)	76 (165/218)
			Slope of enhancement	0.016	93 (124/133)	49 (42/85)	76 (166/218)
			SUV <sub>max</sub>	2	89 (119/133)	31 (26/85)	67 (145/218)
Ohno Y, et al. [20]	320-detector row CT	Lymph node metastasis in NSCLC analyzed per node	Total perfusion (mL/100 mL/min) calculated with slope of enhancement dual-input maximum slope method	58	54.2 (32/59)	89.8 (53/59)	72.0 (85/118)
			Systemic arterial perfusion (mL/100 mL/min) calculated with dual-input maximum slope method	4.1	98.3 (58/59)	56.4 (51/59)	92.4 (109/118)
			Permeability surface (mL/100 mL/min) assessed with Patlak plot method	8.7	50.8 (30/59)	94.9 (56/59)	72.9 (86/118)
			Distribution volume (mL/100 mL) assessed with Patlak plot method	0.37	84.7 (50/59)	44.1 (26/59)	64.34 (76/118)
			SUV <sub>max</sub>	2.9	74.6 (44/59)	91.5 (54/559)	83.1 (98/118)
	FDG-PET/CT						

Table 3. Cont.

Authors	Method	Target	Parameters	Cutoff Values (HU)	SE (%)	SP (%)	AC (%)
Seki S, et al. [22]	320-detector row CT	Therapeutic outcome prediction for NSCLC	Total perfusion (mL/100 mL/min) calculated with dual-input maximum slope method	29.2	78.3 (18/23)	85 (17/20)	81.4 (35/43)
			Pulmonary arterial perfusion (mL/100 mL/min) calculated with dual-input maximum slope method	15.5	65.2 (15/23)	80 (16/20)	72.1 (31/43)
			Systemic arterial perfusion (mL/100 mL/min) calculated with dual-input maximum slope method	11	82.6 (19/23)	80 (16/20)	81.4 (35/43)
	Dynamic first-pass CE-perfusion MRI at 3T system		Total perfusion (mL/100 mL/min) calculated with dual-input maximum slope method	37.5	69.6 (16/23)	95 (19/20)	81.4 (35/43)
			Pulmonary arterial perfusion (mL/100 mL/min) calculated with dual-input maximum slope method	16.3	65.2 (15/23)	80 (16/20)	72.1 (35/43)
			Systemic arterial perfusion (mL/100 mL/min) calculated with dual-input maximum slope method	16.5	82.6 (19/23)	80 (16/20)	81.4 (35/43)
			FDG-PET/CT	SUV <sub>max</sub>	5.7	87.0 (20/23)	76.9 (14/20)

SE: sensitivity, SP: specificity, AC: accuracy, NSCLC: non-small-cell lung cancer; number following author's name corresponds to number in References.

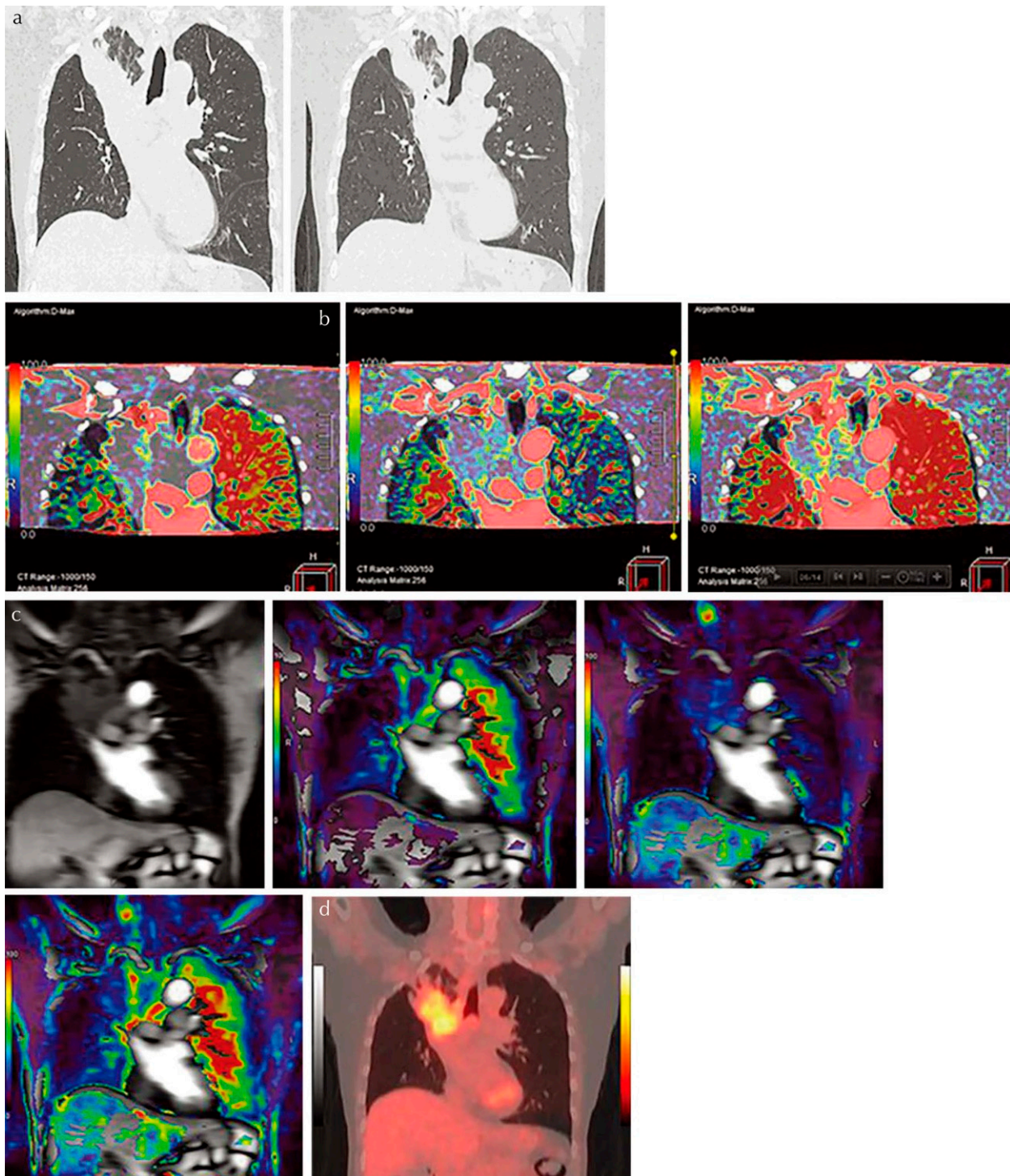


**Figure 3.** An 81-year-old male patient with squamous cell carcinoma treated with chemoradiotherapy and assessed as NC. Progression-free and overall survivals at 15 and 24 months (permission from reference [22]). (a) Thin-section MPR image derived from thin-section CT data (L to R: MPR images obtained pre- and post-treatment at lung window setting) show lung cancer in the right upper lobe. This case was assessed as NC according to response evaluation criteria for solid tumors (RECIST ver.1.1). (b) Perfusion maps derived from dynamic first-pass CE-perfusion area-detector CT assessed with the dual-input maximum slope method (L to R: pulmonary arterial perfusion, systemic arterial perfusion, and total perfusion maps) for the same targeted lesion. Pulmonary arterial perfusion, systemic arterial perfusion, and total perfusion were 13.6, 18.9, and 32.5 mL/100 mL/min, respectively.

This case was assessed as a RECIST-based non-responder for systemic arterial and total perfusions and as true positive. (c) Source image and perfusion maps obtained with dynamic first-pass CE-perfusion MR imaging assessed with the dual-input maximum slope method (L to R: source image, pulmonary arterial perfusion, systemic arterial perfusion, and total perfusion maps) for the same targeted lesion. Pulmonary arterial perfusion, systemic arterial perfusion, and total perfusion were 9.2, 28.9, and 38.1 mL/100 mL/min, respectively. This case was also assessed as a RECIST-based non-responder for systemic arterial and total perfusions and as true positive. However, this case was evaluated as responder and as false positive based on pulmonary arterial perfusion findings. (d) PET/CT shows high uptake of 2-[fluorine-18]-fluoro-2-deoxy-d-glucose, and  $SUV_{max}$  was evaluated as 4.7. This case was evaluated as a RECIST-responder and assessed as false negative. PR, partial response; MPR, multiplanar reformatted; RECIST, Response Evaluation Criteria in Solid Tumors; CE, contrast-enhanced; SUV, standardized uptake value; PET, positron emission tomography.

#### 4.4. Ventilation Assessment

Although the potential of Xe or krypton (Kr) to function as gas contrast media has been known since the 1960s [93–95], they were not academically or clinically used for pulmonary functional imaging until 2008. Oxygen-enhanced MRI and hyperpolarized noble gas MRI were reported to be useful for ventilation-based pulmonary functional imaging in the late 1990s [65–70]. For this reason, Xe- or Kr-enhanced ventilation CTs have mainly been used for pulmonary functional imaging for in vitro or in vivo studies after the clinical installation of DECT since 2008 [67,68,73,87,96–111]. Since that time, DECT has been mainly used by dual-source CT systems for patients with COPD or asthma [67,68,73,87,96–106]. However, no studies on the use of ADCT for Xe-enhanced DECT were published until 2023. In contrast to DECT, subtraction ADCT was demonstrated to be as effective as subtraction CT for the visualization of xenon enhancement for in vitro or in vivo studies and for pulmonary functional loss evaluation in comparison with the use of DECT or Kr-81m ventilation SPECT/CT for in vivo studies [107–111]. Moreover, these in vivo studies have demonstrated the potential of Xe-enhanced subtraction ADCT for regional ventilation evaluation or therapeutic effect assessment for smokers, COPD patients, asthmatics, or lung cancer patients [107–111] (Figure 4).

In addition, inspiratory and expiratory (inspiratory/expiratory) Xe-enhanced subtraction CT with hybrid-type IR has been found to be effective for the assessment of the regional ventilation changes in lung cancer patients due to smoking-related COPD or surgical treatment [110,111]. Although Xe-enhanced subtraction ADCT as well as DECT with dual-source CT are considered to be useful for pulmonary ventilation imaging, cold Xe or Kr has currently not been approved as contrast media for ventilation CT because they were only approved as contrast media for brain CT by the United States Food and Drug Administration, the Japan Pharmaceuticals and Medical Devices Agency, or regulatory authorities in other countries. It is, therefore, vital to obtain, in the near future, the regulatory approval of Xe and Kr as gas contrast media for pulmonary functional imaging, whether Xe-enhanced subtraction ADCT or DECT with dual-source CT are applied.

#### 4.5. Biomechanical Evaluation

Pulmonary functional imaging has been recommended as having the potential to estimate lung compliance by tracking voxel motion at full inspiration (total lung capacity) and at full expiration (residual volume) by means of inspiratory/expiratory CT or MRI [67–70,112]. Moreover, lung compliance estimates derived from free-breathing and static-volume 4D CT and 4D MRI can be obtained by using deformable image registration [67–70,113–123]. Regarding the use of ADCT for the evaluation of lung biomechanics, the ACTIVE study group has published in vitro and in vivo studies of the capability of dynamic 4D ADCT to evaluate regional lung biomechanics and pleural invasion in lung cancer patients as well as air trapping or air flow limitations [115–123]. Moreover, it is now

possible to generate whole lung 4D ADCT images with a proprietary software provided by Canon Medical Systems and, in the near future, to begin to evaluate the efficacy of 4D ADCT as a new system for pulmonary functional imaging.

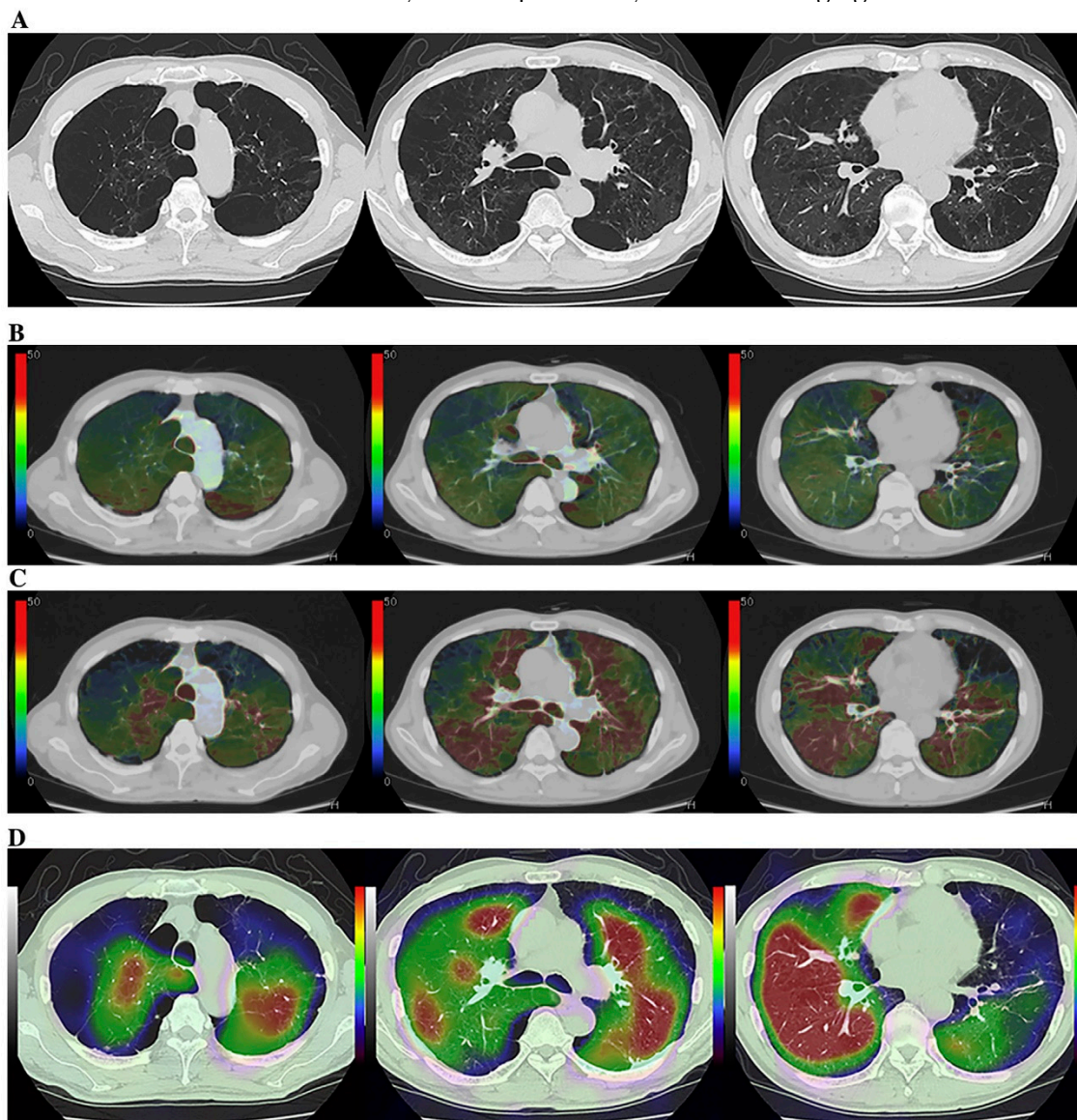


**Figure 4.** A 75-year-old male smoker with “Moderate COPD” (58 pack-years, FEV1/FVC%: 55%, %FEV1: 58%) (permission from reference [108]). (A) (L to R: cranial to caudal): Thin-section CT shows a heterogeneously distributed low attenuation area due to pulmonary emphysema. (B) (L to R: cranial to caudal): DECT shows heterogeneous xenon enhancement within the lung and areas of reduced xenon enhancements corresponding well to the distribution of the areas of low attenuation. Total ventilation defect score was 66, and functional lung volume was 65.8%. (C) (L to R: cranial to caudal): Subtraction CT shows heterogeneous xenon enhancement within the lung and areas of reduced xenon enhancement corresponding well to the distribution of the areas of low attenuation. Total ventilation defect score was 88, and functional lung volume was 53.7%. (D) (L to R: cranial to caudal): Co-registered Kr-81m ventilation SPECT/CT shows markedly heterogeneous uptakes within the lung. Regional uptakes correspond well to areas of low attenuation. Total ventilation defect score was 84, and functional lung volume was 55.8%. Regional uptakes of Kr-81m show better correspondence to xenon enhancement on subtraction CT than on DECT.

## 5. Conclusions

ADCT merits consideration as a useful tool for pulmonary functional imaging not only to evaluate pulmonary morphology but also, with various techniques, to directly evaluate pulmonary function. This system has been clinically tested as an upright CT system at our institution (Figure 5).



**Figure 5.** The first installed and clinically available upright CT with area-detector CT system in Fujita Health University Hospital.

Moreover, it can be expected that some additional technical enhancements will be introduced in this decade on the basis of future studies using newly developed X-ray tubes, detectors, reconstruction methods, or other new technologies. When considering the future advancements of ADCT, faster rotation speed of the X-ray tube, higher isotropic resolution and larger image matrices for ultra- or super-high-resolution CT imaging, faster image processing, and computer-aided diagnosis or artificial intelligence tools are warranted to open new imaging methods for not only oncologic but also pulmonary functional imaging. Therefore, ADCT can be currently used as a standard pulmonary functional imaging tool in routine clinical practice but may soon lead to new pulmonary functional imaging functions.

**Funding:** This work was financially and technically supported by the Canon Medical Systems Corporation.

**Institutional Review Board Statement:** Not applicable.

**Informed Consent Statement:** Not applicable.

**Data Availability Statement:** Not applicable.

**Conflicts of Interest:** Prof. Ohno, Dr. Nagata and Prof. Toyama have research grants from Canon Medical Systems Corporation, Smoking Research Foundation and Japan Society for the Promotion of Science. Prof. Ozawa and Dr. Ueda have research grants from Japan Society for the Promotion of Science.

## References

1. Hu, H. Multi-slice helical CT: Scan and reconstruction. *Med. Phys.* **1999**, *26*, 5–18. [[CrossRef](#)] [[PubMed](#)]
2. Funabashi, N.; Yoshida, K.; Tadokoro, H.; Nakagawa, K.; Komiyama, N.; Odaka, K.; Tsunoo, T.; Mori, S.; Tanada, S.; Endo, M.; et al. Cardiovascular Circulation and Hepatic Perfusion of Pigs in 4-Dimensional Films Evaluated by 256-Slice Cone-Beam Computed Tomography. *Circ. J.* **2005**, *69*, 585–589. [[CrossRef](#)] [[PubMed](#)]
3. Kandel, S.; Kloeters, C.; Meyer, H.; Hein, P.; Hilbig, A.; Rogalla, P. Whole-organ perfusion of the pancreas using dynamic volume CT in patients with primary pancreas carcinoma: Acquisition technique, post-processing and initial results. *Eur. Radiol.* **2009**, *19*, 2641–2646. [[CrossRef](#)]
4. Kanda, T.; Yoshikawa, T.; Ohno, Y.; Kanata, N.; Koyama, H.; Nogami, M.; Takenaka, D.; Sugimura, K. Hepatic computed tomography perfusion: Comparison of maximum slope and dual-input single-compartment methods. *Jpn. J. Radiol.* **2010**, *28*, 714–719. [[CrossRef](#)]
5. Ohno, Y.; Koyama, H.; Matsumoto, K.; Onishi, Y.; Takenaka, D.; Fujisawa, Y.; Yoshikawa, T.; Konishi, M.; Maniwa, Y.; Nishimura, Y.; et al. Differentiation of Malignant and Benign Pulmonary Nodules with Quantitative First-Pass 320-Detector Row Perfusion CT versus FDG PET/CT. *Radiology* **2011**, *258*, 599–609. [[CrossRef](#)]
6. Vavere, A.L.; Simon, G.G.; George, R.T.; Rochitte, C.E.; Arai, A.; Miller, J.M.; Di Carli, M.; Arbab-Zadeh, A.; Dewey, M.; Niinuma, H.; et al. Diagnostic performance of combined noninvasive coronary angiography and myocardial perfusion imaging using 320 row detector computed tomography: Design and implementation of the CORE320 multicenter, multinational diagnostic study. *J. Cardiovasc. Comput. Tomogr.* **2011**, *5*, 370–381. [[CrossRef](#)]
7. Kanda, T.; Yoshikawa, T.; Ohno, Y.; Kanata, N.; Koyama, H.; Takenaka, D.; Sugimura, K. CT hepatic perfusion measurement: Comparison of three analytic methods. *Eur. J. Radiol.* **2012**, *81*, 2075–2079. [[CrossRef](#)]
8. Kanda, T.; Yoshikawa, T.; Ohno, Y.; Fujisawa, Y.; Kanata, N.; Yamaguchi, M.; Seo, Y.; Yano, Y.; Koyama, H.; Kitajima, K.; et al. Perfusion measurement of the whole upper abdomen of patients with and without liver diseases: Initial experience with 320-detector row CT. *Eur. J. Radiol.* **2012**, *81*, 2470–2475. [[CrossRef](#)]
9. Negi, N.; Yoshikawa, T.; Ohno, Y.; Somiya, Y.; Sekitani, T.; Sugihara, N.; Koyama, H.; Kanda, T.; Kanata, N.; Murakami, T.; et al. Hepatic CT perfusion measurements: A feasibility study for radiation dose reduction using new image reconstruction method. *Eur. J. Radiol.* **2012**, *81*, 3048–3054. [[CrossRef](#)]
10. Cerci, R.J.; Arbab-Zadeh, A.; George, R.T.; Miller, J.M.; Vavere, A.L.; Mehra, V.; Yoneyama, K.; Texter, J.; Foster, C.; Guo, W.; et al. Aligning Coronary Anatomy and Myocardial Perfusion Territories: An algorithm for the CORE320 multicenter study. *Circ. Cardiovasc. Imaging* **2012**, *5*, 587–595. [[CrossRef](#)]
11. Nasis, A.; Ko, B.S.; Leung, M.C.; Antonis, P.R.; Nandurkar, D.; Wong, D.T.; Kyi, L.; Cameron, J.D.; Troupis, J.M.; Meredith, I.T.; et al. Diagnostic accuracy of combined coronary angiography and adenosine stress myocardial perfusion imaging using 320-detector computed tomography: Pilot study. *Eur. Radiol.* **2013**, *23*, 1812–1821. [[CrossRef](#)] [[PubMed](#)]
12. Ohno, Y.; Nishio, M.; Koyama, H.; Fujisawa, Y.; Yoshikawa, T.; Matsumoto, S.; Sugimura, K. Comparison of Quantitatively Analyzed Dynamic Area-Detector CT Using Various Mathematic Methods With FDG PET/CT in Management of Solitary Pulmonary Nodules. *AJR Am. J. Roentgenol.* **2013**, *200*, W593–W602. [[CrossRef](#)]
13. Rochitte, C.E.; George, R.T.; Chen, M.Y.; Arbab-Zadeh, A.; Dewey, M.; Miller, J.M.; Niinuma, H.; Yoshioka, K.; Kitagawa, K.; Nakamori, S.; et al. Computed tomography angiography and perfusion to assess coronary artery stenosis causing perfusion defects by single photon emission computed tomography: The CORE320 study. *Eur. Hear. J.* **2013**, *35*, 1120–1130. [[CrossRef](#)]
14. Ohno, Y.; Nishio, M.; Koyama, H.; Miura, S.; Yoshikawa, T.; Matsumoto, S.; Sugimura, K. Dynamic Contrast-Enhanced CT and MRI for Pulmonary Nodule Assessment. *Am. J. Roentgenol.* **2014**, *202*, 515–529. [[CrossRef](#)] [[PubMed](#)]
15. Ohno, Y.; Nishio, M.; Koyama, H.; Seki, S.; Tsubakimoto, M.; Fujisawa, Y.; Yoshikawa, T.; Matsumoto, S.; Sugimura, K. Solitary Pulmonary Nodules: Comparison of Dynamic First-Pass Contrast-enhanced Perfusion Area-Detector CT, Dynamic First-Pass Contrast-enhanced MR Imaging, and FDG PET/CT. *Radiology* **2015**, *274*, 563–575. [[CrossRef](#)] [[PubMed](#)]
16. Ohno, Y.; Koyama, H.; Fujisawa, Y.; Yoshikawa, T.; Inokawa, H.; Sugihara, N.; Seki, S.; Sugimura, K. Hybrid Type iterative reconstruction method vs. filter back projection method: Capability for radiation dose reduction and perfusion assessment on dynamic first-pass contrast-enhanced perfusion chest area-detector CT. *Eur. J. Radiol.* **2016**, *85*, 164–175. [[CrossRef](#)]
17. Ohno, Y.; Koyama, H.; Fujisawa, Y.; Yoshikawa, T.; Seki, S.; Sugihara, N.; Sugimura, K. Dynamic contrast-enhanced perfusion area detector CT for non-small cell lung cancer patients: Influence of mathematical models on early prediction capabilities for treatment response and recurrence after chemoradiotherapy. *Eur. J. Radiol.* **2016**, *85*, 176–186. [[CrossRef](#)] [[PubMed](#)]
18. Ohno, Y.; Koyama, H.; Lee, H.Y.; Miura, S.; Yoshikawa, T.; Sugimura, K. Contrast-enhanced CT- and MRI-based perfusion assessment for pulmonary diseases: Basics and clinical applications. *Diagn. Interv. Radiol.* **2016**, *22*, 407–421. [[CrossRef](#)]

19. Ohno, Y.; Fujisawa, Y.; Koyama, H.; Kishida, Y.; Seki, S.; Sugihara, N.; Yoshikawa, T. Dynamic contrast-enhanced perfusion area-detector CT assessed with various mathematical models: Its capability for therapeutic outcome prediction for non-small cell lung cancer patients with chemoradiotherapy as compared with that of FDG-PET/CT. *Eur. J. Radiol.* **2017**, *86*, 83–91. [[CrossRef](#)] [[PubMed](#)]
20. Ohno, Y.; Fujisawa, Y.; Sugihara, N.; Kishida, Y.; Seki, S.; Koyama, H.; Yoshikawa, T. Dynamic Contrast-Enhanced Perfusion Area-Detector CT: Preliminary Comparison of Diagnostic Performance for N Stage Assessment With FDG PET/CT in Non-Small Cell Lung Cancer. *AJR Am. J. Roentgenol.* **2017**, *209*, W253–W262. [[CrossRef](#)]
21. Ohno, Y.; Fujisawa, Y.; Yui, M.; Takenaka, D.; Koyama, H.; Sugihara, N.; Yoshikawa, T. Solitary pulmonary nodule: Comparison of quantitative capability for differentiation and management among dynamic CE-perfusion MRI at 3 T system, dynamic CE-perfusion ADCT and FDG-PET/CT. *Eur. J. Radiol.* **2019**, *115*, 22–30. [[CrossRef](#)]
22. Seki, S.; Fujisawa, Y.; Yui, M.; Kishida, Y.; Koyama, H.; Ohyu, S.; Sugihara, N.; Yoshikawa, T.; Ohno, Y. Dynamic Contrast-enhanced Area-detector CT vs Dynamic Contrast-enhanced Perfusion MRI vs FDG-PET/CT: Comparison of Utility for Quantitative Therapeutic Outcome Prediction for NSCLC Patients Undergoing Chemoradiotherapy. *Magn. Reson. Med. Sci.* **2020**, *19*, 29–39. [[CrossRef](#)]
23. Murayama, K.; Smit, E.J.; Prokop, M.; Ikeda, Y.; Fujii, K.; Nakahara, I.; Hanamatsu, S.; Katada, K.; Ohno, Y.; Toyama, H. A Bayesian estimation method for cerebral blood flow measurement by area-detector CT perfusion imaging. *Neuroradiology* **2022**, *65*, 65–75. [[CrossRef](#)]
24. Kubo, T.; Lin, P.-J.P.; Stiller, W.; Takahashi, M.; Kauczor, H.-U.; Ohno, Y.; Hatabu, H. Radiation Dose Reduction in Chest CT: A Review. *AJR Am. J. Roentgenol.* **2008**, *190*, 335–343. [[CrossRef](#)] [[PubMed](#)]
25. Kubo, T.; Ohno, Y.; Gautam, S.; Lin, P.-J.P.; Kauczor, H.-U.; Hatabu, H.; iLEAD Study Group. Use of 3D Adaptive Raw-Data Filter in CT of the Lung: Effect on Radiation Dose Reduction. *Am. J. Roentgenol.* **2008**, *191*, 1071. [[CrossRef](#)] [[PubMed](#)]
26. Matsumoto, K.; Ohno, Y.; Koyama, H.; Kono, A.; Inokawa, H.; Onishi, Y.; Nogami, M.; Takenaka, D.; Araki, T.; Sugimura, K. 3D automatic exposure control for 64-detector row CT: Radiation dose reduction in chest phantom study. *Eur. J. Radiol.* **2011**, *77*, 522–527. [[CrossRef](#)] [[PubMed](#)]
27. Ohno, Y.; Takenaka, D.; Kanda, T.; Yoshikawa, T.; Matsumoto, S.; Sugihara, N.; Sugimura, K. Adaptive Iterative Dose Reduction Using 3D Processing for Reduced- and Low-Dose Pulmonary CT: Comparison With Standard-Dose CT for Image Noise Reduction and Radiological Findings. *AJR Am. J. Roentgenol.* **2012**, *199*, W477–W485. [[CrossRef](#)]
28. Kubo, T.; Ohno, Y.; Kauczor, H.U.; Hatabu, H. Radiation dose reduction in chest CT—Review of available options. *Eur. J. Radiol.* **2014**, *83*, 1953–1961. [[CrossRef](#)] [[PubMed](#)]
29. Kubo, T.; Ohno, Y.; Seo, J.B.; Yamashiro, T.; Kalender, W.A.; Lee, C.H.; Lynch, D.A.; Kauczor, H.-U.; Hatabu, H. Securing safe and informative thoracic CT examinations—Progress of radiation dose reduction techniques. *Eur. J. Radiol.* **2017**, *86*, 313–319. [[CrossRef](#)]
30. Ohno, Y.; Koyama, H.; Seki, S.; Kishida, Y.; Yoshikawa, T. Radiation dose reduction techniques for chest CT: Principles and clinical results. *Eur. J. Radiol.* **2019**, *111*, 93–103. [[CrossRef](#)]
31. Ohno, Y.; Yaguchi, A.; Okazaki, T.; Aoyagi, K.; Yamagata, H.; Sugihara, N.; Koyama, H.; Yoshikawa, T.; Sugimura, K. Comparative evaluation of newly developed model-based and commercially available hybrid-type iterative reconstruction methods and filter back projection method in terms of accuracy of computer-aided volumetry (CADv) for low-dose CT protocols in phantom study. *Eur. J. Radiol.* **2016**, *85*, 1375–1382. [[CrossRef](#)] [[PubMed](#)]
32. Wu, D.; Kim, K.; El Fakhri, G.; Li, Q. Iterative Low-Dose CT Reconstruction With Priors Trained by Artificial Neural Network. *IEEE Trans. Med. Imaging* **2017**, *36*, 2479–2486. [[CrossRef](#)] [[PubMed](#)]
33. Yang, Q.; Yan, P.; Zhang, Y.; Yu, H.; Shi, Y.; Mou, X.; Kalra, M.K.; Zhang, Y.; Sun, L.; Wang, G. Low-Dose CT Image Denoising Using a Generative Adversarial Network With Wasserstein Distance and Perceptual Loss. *IEEE Trans. Med. Imaging* **2018**, *37*, 1348–1357. [[CrossRef](#)]
34. Higaki, T.; Nakamura, Y.; Tatsugami, F.; Nakaura, T.; Awai, K. Improvement of image quality at CT and MRI using deep learning. *Jpn. J. Radiol.* **2019**, *37*, 73–80. [[CrossRef](#)] [[PubMed](#)]
35. Bao, P.; Sun, H.; Wang, Z.; Zhang, Y.; Xia, W.; Yang, K.; Chen, W.; Chen, M.; Xi, Y.; Niu, S.; et al. Convolutional Sparse Coding for Compressed Sensing CT Reconstruction. *IEEE Trans. Med. Imaging* **2019**, *38*, 2607–2619. [[CrossRef](#)] [[PubMed](#)]
36. Matsukiyo, R.; Ohno, Y.; Matsuyama, T.; Nagata, H.; Kimata, H.; Ito, Y.; Ogawa, Y.; Murayama, K.; Kato, R.; Toyama, H. Deep learning-based and hybrid-type iterative reconstructions for CT: Comparison of capability for quantitative and qualitative image quality improvements and small vessel evaluation at dynamic CE-abdominal CT with ultra-high and standard resolutions. *Jpn. J. Radiol.* **2021**, *39*, 186–197. [[CrossRef](#)]
37. Koetzier, L.R.; Mastrodicasa, D.; Szczykutowicz, T.P.; van der Werf, N.R.; Wang, A.S.; Sandfort, V.; van der Molen, A.J.; Fleischmann, D.; Willeminck, M.J. Deep Learning Image Reconstruction for CT: Technical Principles and Clinical Prospects. *Radiology* **2023**, *306*, e221257. [[CrossRef](#)]
38. Yamashiro, T.; Miyara, T.; Honda, O.; Kamiya, H.; Murata, K.; Ohno, Y.; Tomiyama, N.; Moriya, H.; Koyama, M.; Noma, S.; et al. Adaptive Iterative Dose Reduction Using Three Dimensional Processing (AIDR3D) Improves Chest CT Image Quality and Reduces Radiation Exposure. *PLoS ONE* **2014**, *9*, e105735. [[CrossRef](#)]



39. Nagatani, Y.; Takahashi, M.; Murata, K.; Ikeda, M.; Yamashiro, T.; Miyara, T.; Koyama, H.; Koyama, M.; Sato, Y.; Moriya, H.; et al. Lung nodule detection performance in five observers on computed tomography (CT) with adaptive iterative dose reduction using three-dimensional processing (AIDR 3D) in a Japanese multicenter study: Comparison between ultra-low-dose CT and low-dose CT by receiver-operating characteristic analysis. *Eur. J. Radiol.* **2015**, *84*, 1401–1412. [[CrossRef](#)]
40. Nagatani, Y.; Takahashi, M.; Ikeda, M.; Yamashiro, T.; Koyama, H.; Koyama, M.; Moriya, H.; Noma, S.; Tomiyama, N.; Ohno, Y.; et al. Sub-solid Nodule Detection Performance on Reduced-dose Computed Tomography with Iterative Reduction. *Acad. Radiol.* **2017**, *24*, 995–1007. [[CrossRef](#)]
41. Chen-Mayer, H.H.; Fuld, M.K.; Hoppel, B.; Judy, P.F.; Sieren, J.P.; Guo, J.; Lynch, D.A.; Possolo, A.; Fain, S.B. Standardizing CT lung density measure across scanner manufacturers. *Med. Phys.* **2017**, *44*, 974–985. [[CrossRef](#)] [[PubMed](#)]
42. Ohno, Y.; Fujisawa, Y.; Fujii, K.; Sugihara, N.; Kishida, Y.; Seki, S.; Yoshikawa, T. Effects of acquisition method and reconstruction algorithm for CT number measurement on standard-dose CT and reduced-dose CT: A QIBA phantom study. *Jpn. J. Radiol.* **2019**, *37*, 399–411. [[CrossRef](#)] [[PubMed](#)]
43. Ohno, Y.; Akino, N.; Fujisawa, Y.; Kimata, H.; Ito, Y.; Fujii, K.; Kataoka, Y.; Ida, Y.; Oshima, Y.; Hamabuchi, N.; et al. Comparison of lung CT number and airway dimension evaluation capabilities of ultra-high-resolution CT, using different scan modes and reconstruction methods including deep learning reconstruction, with those of multi-detector CT in a QIBA phantom study. *Eur. Radiol.* **2023**, *33*, 368–379. [[CrossRef](#)] [[PubMed](#)]
44. Nishio, M.; Matsumoto, S.; Ohno, Y.; Sugihara, N.; Inokawa, H.; Yoshikawa, T.; Sugimura, K. Emphysema Quantification by Low-Dose CT: Potential Impact of Adaptive Iterative Dose Reduction Using 3D Processing. *AJR Am. J. Roentgenol.* **2012**, *199*, 595–601. [[CrossRef](#)]
45. Nishio, M.; Matsumoto, S.; Seki, S.; Koyama, H.; Ohno, Y.; Fujisawa, Y.; Sugihara, N.; Yoshikawa, T.; Sugimura, K. Emphysema quantification on low-dose CT using percentage of low-attenuation volume and size distribution of low-attenuation lung regions: Effects of adaptive iterative dose reduction using 3D processing. *Eur. J. Radiol.* **2014**, *83*, 2268–2276. [[CrossRef](#)]
46. Nishio, M.; Koyama, H.; Ohno, Y.; Negi, N.; Seki, S.; Yoshikawa, T.; Sugimura, K. Emphysema Quantification Using Ultralow-Dose CT With Iterative Reconstruction and Filtered Back Projection. *AJR Am. J. Roentgenol.* **2016**, *206*, 1184–1192. [[CrossRef](#)]
47. Ohno, Y.; Aoyagi, K.; Chen, Q.; Sugihara, N.; Iwasawa, T.; Okada, F.; Aoki, T. Comparison of computer-aided detection (CADe) capability for pulmonary nodules among standard-, reduced- and ultra-low-dose CTs with and without hybrid type iterative reconstruction technique. *Eur. J. Radiol.* **2018**, *100*, 49–57. [[CrossRef](#)]
48. McDonough, J.E.; Yuan, R.; Suzuki, M.; Seyednejad, N.; Elliott, W.M.; Sanchez, P.G.; Wright, A.C.; Geffer, W.B.; Litzky, L.; Coxson, H.O.; et al. Small-Airway Obstruction and Emphysema in Chronic Obstructive Pulmonary Disease. *N. Engl. J. Med.* **2011**, *365*, 1567–1575. [[CrossRef](#)]
49. Hackx, M.; Bankier, A.A.; Gevenois, P.A. Chronic Obstructive Pulmonary Disease: CT Quantification of Airways Disease. *Radiology* **2012**, *265*, 34–48. [[CrossRef](#)]
50. Lynch, D.A.; Al-Qaisi, M.A. Quantitative Computed Tomography in Chronic Obstructive Pulmonary Disease. *J. Thorac. Imaging* **2013**, *28*, 284–290. [[CrossRef](#)]
51. Kim, S.S.; Seo, J.B.; Lee, H.Y.; Nevrekar, D.V.; Forssen, A.V.; Crapo, J.D.; Schroeder, J.D.; Lynch, D.A.; Moore, C.M.; Wilson, C.; et al. Chronic Obstructive Pulmonary Disease: Lobe-based Visual Assessment of Volumetric CT by Using Standard Images—Comparison with Quantitative CT and Pulmonary Function Test in the COPDGene Study. *Radiology* **2013**, *266*, 626–635. [[CrossRef](#)] [[PubMed](#)]
52. Hague, C.J.; Krowchuk, N.; Alhassan, D.; Ho, K.; Leipsic, J.; Sin, D.D.; Mayo, J.R.; Coxson, H.O. Qualitative and Quantitative Assessment of Smoking-related Lung Disease: Effect of iterative reconstruction on low-dose computed tomographic examinations. *J. Thorac. Imaging* **2014**, *29*, 350–356. [[CrossRef](#)] [[PubMed](#)]
53. Nambu, A.; Zach, J.; Schroeder, J.; Jin, G.; Kim, S.S.; Kim, Y.-I.; Schnell, C.; Bowler, R.; Lynch, D.A. Quantitative computed tomography measurements to evaluate airway disease in chronic obstructive pulmonary disease: Relationship to physiological measurements, clinical index and visual assessment of airway disease. *Eur. J. Radiol.* **2016**, *85*, 2144–2151. [[CrossRef](#)] [[PubMed](#)]
54. Hoffman, E.A.; Lynch, D.A.; Barr, R.G.; van Beek, E.J.; Parraga, G.; IWPF Investigators. Pulmonary CT and MRI phenotypes that help explain chronic pulmonary obstruction disease pathophysiology and outcomes. *J. Magn. Reson. Imaging* **2015**, *43*, 544–557. [[CrossRef](#)] [[PubMed](#)]
55. Kauczor, H.-U.; Wielpütz, M.O.; Jobst, B.J.; Weinheimer, O.; Gompelmann, D.; Herth, F.J.; Heussel, C.P. Computed Tomography Imaging for Novel Therapies of Chronic Obstructive Pulmonary Disease. *J. Thorac. Imaging* **2019**, *34*, 202–213. [[CrossRef](#)] [[PubMed](#)]
56. Petousi, N.; Talbot, N.P.; Pavord, I.; A Robbins, P. Measuring lung function in airways diseases: Current and emerging techniques. *Thorax* **2019**, *74*, 797–805. [[CrossRef](#)]
57. Goldin, J.G. The Emerging Role of Quantification of Imaging for Assessing the Severity and Disease Activity of Emphysema, Airway Disease, and Interstitial Lung Disease. *Respiration* **2021**, *100*, 277–290. [[CrossRef](#)]
58. Koyama, H.; Ohno, Y.; Yamazaki, Y.; Onishi, Y.; Takenaka, D.; Yoshikawa, T.; Nishio, M.; Matsumoto, S.; Murase, K.; Nishimura, Y.; et al. Quantitative bronchial luminal volumetric assessment of pulmonary function loss by thin-section MDCT in pulmonary emphysema patients. *Eur. J. Radiol.* **2012**, *81*, 384–388. [[CrossRef](#)]

59. Koyama, H.; Ohno, Y.; Nishio, M.; Matsumoto, S.; Sugihara, N.; Yoshikawa, T.; Seki, S.; Sugimura, K. Iterative reconstruction technique vs filter back projection: Utility for quantitative bronchial assessment on low-dose thin-section MDCT in patients with/without chronic obstructive pulmonary disease. *Eur. Radiol.* **2014**, *24*, 1860–1867. [[CrossRef](#)]
60. Yamashiro, T.; Miyara, T.; Honda, O.; Tomiyama, N.; Ohno, Y.; Noma, S.; Murayama, S. Iterative reconstruction for quantitative computed tomography analysis of emphysema: Consistent results using different tube currents. *Int. J. Chronic Obstr. Pulm. Dis.* **2015**, *10*, 321–327. [[CrossRef](#)]
61. Ohno, Y.; Aoyagi, K.; Takenaka, D.; Yoshikawa, T.; Ikezaki, A.; Fujisawa, Y.; Murayama, K.; Hattori, H.; Toyama, H. Machine learning for lung CT texture analysis: Improvement of inter-observer agreement for radiological finding classification in patients with pulmonary diseases. *Eur. J. Radiol.* **2021**, *134*, 109410. [[CrossRef](#)] [[PubMed](#)]
62. Ohno, Y.; Aoyagi, K.; Arakita, K.; Doi, Y.; Kondo, M.; Banno, S.; Kasahara, K.; Ogawa, T.; Kato, H.; Hase, R.; et al. Newly developed artificial intelligence algorithm for COVID-19 pneumonia: Utility of quantitative CT texture analysis for prediction of favipiravir treatment effect. *Jpn. J. Radiol.* **2022**, *40*, 800–813. [[CrossRef](#)] [[PubMed](#)]
63. Ohno, Y.; Aoyagi, K.; Takenaka, D.; Yoshikawa, T.; Fujisawa, Y.; Sugihara, N.; Hamabuchi, N.; Hanamatsu, S.; Obama, Y.; Ueda, T.; et al. Machine learning for lung texture analysis on thin-section CT: Capability for assessments of disease severity and therapeutic effect for connective tissue disease patients in comparison with expert panel evaluations. *Acta Radiol.* **2022**, *63*, 1363–1373. [[CrossRef](#)]
64. Uematsu, H.; Ohno, Y.; Hatabu, H. Recent Advances in Magnetic Resonance Perfusion Imaging of the Lung. *Top. Magn. Reson. Imaging* **2003**, *14*, 245–251. [[CrossRef](#)]
65. Matsuoka, S.; Hunsaker, A.R.; Gill, R.R.; Jacobson, F.L.; Ohno, Y.; Patz, S.; Hatabu, H. Functional MR Imaging of the Lung. *Magn. Reson. Imaging Clin. North Am.* **2008**, *16*, 275–289. [[CrossRef](#)] [[PubMed](#)]
66. Ohno, Y.; Koyama, H.; Yoshikawa, T.; Nishio, M.; Matsumoto, S.; Iwasawa, T.; Sugimura, K. Pulmonary Magnetic Resonance Imaging for Airway Diseases. *J. Thorac. Imaging* **2011**, *26*, 301–316. [[CrossRef](#)]
67. Ohno, Y.; Seo, J.B.; Parraga, G.; Lee, K.S.; Geftter, W.B.; Fain, S.B.; Schiebler, M.L.; Hatabu, H. Pulmonary Functional Imaging: Part 1—State-of-the-Art Technical and Physiologic Underpinnings. *Radiology* **2021**, *299*, 508–523. [[CrossRef](#)]
68. Geftter, W.B.; Lee, K.S.; Schiebler, M.L.; Parraga, G.; Seo, J.B.; Ohno, Y.; Hatabu, H. Pulmonary Functional Imaging: Part 2—State-of-the-Art Clinical Applications and Opportunities for Improved Patient Care. *Radiology* **2021**, *299*, 524–538. [[CrossRef](#)]
69. Tanaka, Y.; Ohno, Y.; Hanamatsu, S.; Obama, Y.; Ueda, T.; Ikeda, H.; Iwase, A.; Fukuba, T.; Hattori, H.; Murayama, K.; et al. State-of-the-art MR Imaging for Thoracic Diseases. *Magn. Reson. Med. Sci.* **2022**, *21*, 212–234. [[CrossRef](#)]
70. Ohno, Y.; Hanamatsu, S.; Obama, Y.; Ueda, T.; Ikeda, H.; Hattori, H.; Murayama, K.; Toyama, H. Overview of MRI for pulmonary functional imaging. *Br. J. Radiol.* **2022**, *95*, 20201053. [[CrossRef](#)]
71. Thieme, S.F.; Johnson, T.R.; Reiser, M.F.; Nikolaou, K. Dual-Energy Lung Perfusion Computed Tomography: A Novel Pulmonary Functional Imaging Method. *Semin. Ultrasound, CT MRI* **2010**, *31*, 301–308. [[CrossRef](#)]
72. Chae, E.J.; Song, J.-W.; Krauss, B.; Song, K.-S.; Lee, C.W.; Lee, H.J.; Seo, J.B. Dual-energy Computed Tomography Characterization of Solitary Pulmonary Nodules. *J. Thorac. Imaging* **2010**, *25*, 301–310. [[CrossRef](#)] [[PubMed](#)]
73. Faivre, J.-B.; Pontana, F.; Molinari, F.; Tacelli, N.; Remy, J.; Remy-Jardin, M. Thoracic Applications of Dual Energy. *Semin. Respir. Crit. Care Med.* **2014**, *35*, 064–073. [[CrossRef](#)] [[PubMed](#)]
74. De Santis, D.; Eid, M.; De Cecco, C.N.; Jacobs, B.E.; Albrecht, M.H.; Varga-Szemes, A.; Tesche, C.; Caruso, D.; Laghi, A.; Schoepf, U.J. Dual-Energy Computed Tomography in Cardiothoracic Vascular Imaging. *Radiol. Clin. North Am.* **2018**, *56*, 521–534. [[CrossRef](#)]
75. Vlahos, I.; Jacobsen, M.C.; Godoy, M.C.; Stefanidis, K.; Layman, R.R. Dual-energy CT in pulmonary vascular disease. *Br. J. Radiol.* **2022**, *95*, 20210699. [[CrossRef](#)] [[PubMed](#)]
76. Vulasala, S.S.R.; Wynn, G.C.; Hernandez, M.; Kadambi, I.; Gopireddy, D.R.; Bhosale, P.; Virarkar, M.K. Dual-Energy Imaging of the Chest. *Semin. Ultrasound, CT MRI* **2022**, *43*, 311–319. [[CrossRef](#)]
77. Rapp, J.B.; Biko, D.M.; Siegel, M.J. Dual-Energy CT for Pediatric Thoracic Imaging: A Review. *AJR Am. J. Roentgenol.* **2023**; *Online ahead of print.* [[CrossRef](#)]
78. Piper, J.; Ikeda, Y.; Fujisawa, Y.; Ohno, Y.; Yoshikawa, T.; O’neil, A.; Poole, I. Objective evaluation of the correction by non-rigid registration of abdominal organ motion in low-dose 4D dynamic contrast-enhanced CT. *Phys. Med. Biol.* **2012**, *57*, 1701–1715. [[CrossRef](#)]
79. Grob, D.; Oostveen, L.; Rühaak, J.; Heldmann, S.; Mohr, B.; Michielsen, K.; Dorn, S.; Prokop, M.; Kachelrieß, M.; Brink, M.; et al. Accuracy of registration algorithms in subtraction CT of the lungs: A digital phantom study. *Med. Phys.* **2019**, *46*, 2264–2274. [[CrossRef](#)]
80. Baerends, E.; Oostveen, L.J.; Smit, C.T.; Das, M.; Sechopoulos, I.; Brink, M.; de Lange, F.; Prokop, M. Comparing dual energy CT and subtraction CT on a phantom: Which one provides the best contrast in iodine maps for sub-centimetre details? *Eur. Radiol.* **2018**, *28*, 5051–5059. [[CrossRef](#)]
81. Grob, D.; Oostveen, L.J.; Prokop, M.; Schaefer-Prokop, C.M.; Sechopoulos, I.; Brink, M. Imaging of pulmonary perfusion using subtraction CT angiography is feasible in clinical practice. *Eur. Radiol.* **2019**, *29*, 1408–1414. [[CrossRef](#)] [[PubMed](#)]

82. Tamura, M.; Yamada, Y.; Kawakami, T.; Kataoka, M.; Iwabuchi, Y.; Sugiura, H.; Hashimoto, M.; Nakahara, T.; Okuda, S.; Nakatsuka, S.; et al. Diagnostic accuracy of lung subtraction iodine mapping CT for the evaluation of pulmonary perfusion in patients with chronic thromboembolic pulmonary hypertension: Correlation with perfusion SPECT/CT. *Int. J. Cardiol.* **2017**, *243*, 538–543. [[CrossRef](#)]
83. Dissaux, B.; Le Floch, P.-Y.; Robin, P.; Bourhis, D.; Couturaud, F.; Salaun, P.-Y.; Nonent, M.; Le Roux, P.-Y. Pulmonary perfusion by iodine subtraction maps CT angiography in acute pulmonary embolism: Comparison with pulmonary perfusion SPECT (PASEP trial). *Eur. Radiol.* **2020**, *30*, 4857–4864. [[CrossRef](#)] [[PubMed](#)]
84. Grob, D.; Oostveen, L.J.; Jacobs, C.; Scholten, E.; Prokop, M.; Schaefer-Prokop, C.M.; Sechopoulos, I.; Brink, M. Pulmonary nodule enhancement in subtraction CT and dual-energy CT: A comparison study. *Eur. J. Radiol.* **2021**, *134*, 109443. [[CrossRef](#)] [[PubMed](#)]
85. Schoepf, U.J.; Bruening, R.; Konschitzky, H.; Becker, C.R.; Knez, A.; Weber, J.; Muehling, O.; Herzog, P.; Huber, A.; Haberl, R.; et al. Pulmonary Embolism: Comprehensive Diagnosis by Using Electron-Beam CT for Detection of Emboli and Assessment of Pulmonary Blood Flow. *Radiology* **2000**, *217*, 693–700. [[CrossRef](#)]
86. Herzog, P.; Wildberger, J.E.; Niethammer, M.; Schaller, S.; Schoepf, U. CT perfusion imaging of the lung in pulmonary embolism1. *Acad. Radiol.* **2003**, *10*, 1132–1146. [[CrossRef](#)]
87. Hoffman, E.A. Computed Tomography Studies of Lung Ventilation and Perfusion. *Proc. Am. Thorac. Soc.* **2005**, *2*, 492–498. [[CrossRef](#)] [[PubMed](#)]
88. Ng, Q.-S.; Goh, V.; Fichte, H.; Klotz, E.; Fernie, P.; Saunders, M.I.; Hoskin, P.J.; Padhani, A.R. Lung Cancer Perfusion at Multi-Detector Row CT: Reproducibility of Whole Tumor Quantitative Measurements. *Radiology* **2006**, *239*, 547–553. [[CrossRef](#)]
89. Ng, Q.S.; Goh, V.J.; Klotz, E.; Fichte, H.; Saunders, M.I.; Hoskin, P.J.; Padhani, A.R. Quantitative Assessment of Lung Cancer Perfusion Using MDCT: Does Measurement Reproducibility Improve with Greater Tumor Volume Coverage? *AJR Am. J. Roentgenol.* **2006**, *187*, 1079–1084. [[CrossRef](#)]
90. Sitartchouk, I.; Roberts, H.C.; Pereira, A.M.; Bayanati, H.; Waddell, T.; Roberts, T.P. Computed Tomography Perfusion Using First Pass Methods for Lung Nodule Characterization. *Investig. Radiol.* **2008**, *43*, 349–358. [[CrossRef](#)]
91. Wang, J.; Wu, N.; Cham, M.D.; Song, Y. Tumor Response in Patients With Advanced Non-Small Cell Lung Cancer: Perfusion CT Evaluation of Chemotherapy and Radiation Therapy. *AJR Am. J. Roentgenol.* **2009**, *193*, 1090–1096. [[CrossRef](#)]
92. Li, Y.; Yang, Z.-G.; Chen, T.-W.; Yu, J.-Q.; Sun, J.-Y.; Chen, H.-J. First-pass perfusion imaging of solitary pulmonary nodules with 64-detector row CT: Comparison of perfusion parameters of malignant and benign lesions. *Br. J. Radiol.* **2010**, *83*, 785–790. [[CrossRef](#)]
93. Rockoff, S.D.; Mendelsohn, M.L. Evaluation of xenon as a gaseous roentgenographic contrast material. A preliminary report. *Am. Rev. Respir. Dis.* **1962**, *86*, 434–438. [[CrossRef](#)] [[PubMed](#)]
94. Winkler, S.S.; Holden, J.E.; Sackett, J.F.; Flemming, D.C.; Alexander, S.C. Xenon and Krypton as Radiographic Inhalation Contrast Media With Computerized Tomography: Preliminary Note. *Investig. Radiol.* **1977**, *12*, 19–20. [[CrossRef](#)]
95. Chon, D.; Beck, K.C.; Simon, B.A.; Shikata, H.; Saba, O.I.; Hoffman, E.A. Effect of low-xenon and krypton supplementation on signal/noise of regional CT-based ventilation measurements. *J. Appl. Physiol.* **2007**, *102*, 1535–1544. [[CrossRef](#)]
96. Chae, E.J.; Seo, J.B.; Goo, H.W.; Kim, N.; Song, K.-S.; Lee, S.D.; Hong, S.-J.; Krauss, B. Xenon Ventilation CT with a Dual-Energy Technique of Dual-Source CT: Initial Experience. *Radiology* **2008**, *248*, 615–624. [[CrossRef](#)] [[PubMed](#)]
97. Park, E.-A.; Goo, J.M.; Park, S.J.; Lee, H.J.; Lee, C.H.; Park, C.M.; Yoo, C.-G.; Kim, J.H. Chronic Obstructive Pulmonary Disease: Quantitative and Visual Ventilation Pattern Analysis at Xenon Ventilation CT Performed by Using a Dual-Energy Technique. *Radiology* **2010**, *256*, 985–997. [[CrossRef](#)] [[PubMed](#)]
98. Chae, E.J.; Seo, J.B.; Lee, J.; Kim, N.; Goo, H.W.; Lee, H.J.; Lee, C.W.; Ra, S.W.; Oh, Y.-M.; Cho, Y.S. Xenon Ventilation Imaging Using Dual-Energy Computed Tomography in Asthmatics. *Investig. Radiol.* **2010**, *45*, 354–361. [[CrossRef](#)]
99. Honda, N.; Osada, H.; Watanabe, W.; Nakayama, M.; Nishimura, K.; Krauss, B.; Otani, K. Imaging of Ventilation with Dual-Energy CT during Breath Hold after Single Vital-Capacity Inspiration of Stable Xenon. *Radiology* **2012**, *262*, 262–268. [[CrossRef](#)]
100. Lu, G.M.; Zhao, Y.; Zhang, L.J.; Schoepf, U.J. Dual-Energy CT of the Lung. *AJR Am. J. Roentgenol.* **2012**, *199* (Suppl. S5), S40–S53. [[CrossRef](#)]
101. Park, S.J.; Lee, C.H.; Goo, J.M.; Kim, J.H.; Park, E.-A.; Jung, J.-W.; Park, H.-W.; Cho, S.-H. Quantitative analysis of dynamic airway changes after methacholine and salbutamol inhalation on xenon-enhanced chest CT. *Eur. Radiol.* **2012**, *22*, 2441–2450. [[CrossRef](#)]
102. Kim, W.W.; Lee, C.H.; Goo, J.M.; Park, S.J.; Kim, J.H.; Park, E.-A.; Cho, S.-H. Xenon-Enhanced Dual-Energy CT of Patients With Asthma: Dynamic Ventilation Changes After Methacholine and Salbutamol Inhalation. *AJR Am. J. Roentgenol.* **2012**, *199*, 975–981. [[CrossRef](#)] [[PubMed](#)]
103. Jung, J.-W.; Kwon, J.-W.; Kim, T.-W.; Lee, S.-H.; Kim, K.-M.; Kang, H.-R.; Park, H.-W.; Lee, C.-H.; Goo, J.-M.; Min, K.-U.; et al. New insight into the assessment of asthma using xenon ventilation computed tomography. *Ann. Allergy Asthma Immunol.* **2013**, *111*, 90–95.e2. [[CrossRef](#)] [[PubMed](#)]

104. Kong, X.; Sheng, H.X.; Lu, G.M.; Meinel, F.G.; Dyer, K.T.; Schoepf, U.J.; Zhang, L.J. Xenon-Enhanced Dual-Energy CT Lung Ventilation Imaging: Techniques and Clinical Applications. *Am. J. Roentgenol.* **2014**, *202*, 309–317. [[CrossRef](#)] [[PubMed](#)]
105. Park, H.-W.; Jung, J.-W.; Kim, K.-M.; Kim, T.-W.; Lee, S.-H.; Lee, C.H.; Goo, J.M.; Min, K.-U.; Cho, S.-H. Xenon ventilation computed tomography and the management of asthma in the elderly. *Respirology* **2014**, *19*, 389–395. [[CrossRef](#)] [[PubMed](#)]
106. Hwang, H.J.; Lee, S.M.; Seo, J.B.; Lee, J.S.; Kim, N.; Lee, S.W.; Oh, Y.-M. Visual and Quantitative Assessments of Regional Xenon-Ventilation Using Dual-Energy CT in Asthma-Chronic Obstructive Pulmonary Disease Overlap Syndrome: A Comparison with Chronic Obstructive Pulmonary Disease. *Korean J. Radiol.* **2020**, *21*, 1104–1113. [[CrossRef](#)]
107. Dokuni, R.; Kobayashi, K.; Ohno, Y.; Nagano, T.; Tamura, D.; Umezawa, K.; Katsurada, N.; Nakata, K.; Yamamoto, M.; Tachihara, M.; et al. Effect of Bronchial Thermoplasty on Air Trapping Assessed by Xenon Ventilation Computed Tomography. *Intern. Med.* **2021**, *60*, 2027–2032. [[CrossRef](#)]
108. Ohno, Y.; Yoshikawa, T.; Takenaka, D.; Fujisawa, Y.; Sugihara, N.; Kishida, Y.; Seki, S.; Koyama, H.; Sugimura, K. Xenon-enhanced CT using subtraction CT: Basic and preliminary clinical studies for comparison of its efficacy with that of dual-energy CT and ventilation SPECT/CT to assess regional ventilation and pulmonary functional loss in smokers. *Eur. J. Radiol.* **2017**, *86*, 41–51. [[CrossRef](#)]
109. Ohno, Y.; Fujisawa, Y.; Takenaka, D.; Kaminaga, S.; Seki, S.; Sugihara, N.; Yoshikawa, T. Comparison of Xenon-Enhanced Area-Detector CT and Krypton Ventilation SPECT/CT for Assessment of Pulmonary Functional Loss and Disease Severity in Smokers. *AJR Am. J. Roentgenol.* **2018**, *210*, W45–W53. [[CrossRef](#)]
110. Ohno, Y.; Fujisawa, Y.; Sugihara, N.; Kishida, Y.; Koyama, H.; Seki, S.; Yoshikawa, T. Wash-in/wash-out phase xenon-enhanced area-detector CT (ADCT): Utility for regional ventilation, pulmonary functional loss and clinical stage evaluations of smokers. *Acta Radiol.* **2019**, *60*, 1619–1628. [[CrossRef](#)]
111. Ohno, Y.; Fujisawa, Y.; Yoshikawa, T.; Takenaka, D.; Koyama, H.; Hattori, H.; Murayama, K.; Fujii, K.; Sugihara, N.; Toyama, H. Inspiratory/expiratory xenon-enhanced area-detector CT: Capability for quantitative assessment of lung ventilation changes in surgically treated non-small cell lung cancer patients. *Eur. J. Radiol.* **2021**, *136*, 109574. [[CrossRef](#)]
112. Koyama, H.; Ohno, Y.; Fujisawa, Y.; Seki, S.; Negi, N.; Murakami, T.; Yoshikawa, T.; Sugihara, N.; Nishimura, Y.; Sugimura, K. 3D lung motion assessments on inspiratory/expiratory thin-section CT: Capability for pulmonary functional loss of smoking-related COPD in comparison with lung destruction and air trapping. *Eur. J. Radiol.* **2016**, *85*, 352–359. [[CrossRef](#)] [[PubMed](#)]
113. Sharifi, H.; Brown, S.; McDonald, G.C.; Chetty, I.J.; Zhong, H. 4-Dimensional computed tomography-based ventilation and compliance images for quantification of radiation-induced changes in pulmonary function. *J. Med. Imaging Radiat. Oncol.* **2019**, *63*, 370–377. [[CrossRef](#)] [[PubMed](#)]
114. Guo, J.; Hardie, W.D.; Cleveland, Z.I.; Davidson, C.R.; Xu, X.; Madala, S.K.; Woods, J.C. Longitudinal free-breathing MRI measurement of murine lung physiology in a progressive model of lung fibrosis. *J. Appl. Physiol.* **2019**, *126*, 1138–1149. [[CrossRef](#)] [[PubMed](#)]
115. Yamashiro, T.; Tsubakimoto, M.; Teramoto, R.; Murayama, S.; Nagatani, Y.; Moriya, H.; Sakuma, K.; Tsukagoshi, S.; Inokawa, H.; Kimoto, T. Automated continuous quantitative measurement of proximal airways on dynamic ventilation CT: Initial experience using an ex vivo porcine lung phantom. *Int. J. Chronic Obstr. Pulm. Dis.* **2015**, *10*, 2045–2054. [[CrossRef](#)] [[PubMed](#)]
116. Yamashiro, T.; Moriya, H.; Matsuoka, S.; Nagatani, Y.; Tsubakimoto, M.; Tsuchiya, N.; Murayama, S. Asynchrony in respiratory movements between the pulmonary lobes in patients with COPD: Continuous measurement of lung density by 4-dimensional dynamic-ventilation CT. *Int. J. Chronic Obstr. Pulm. Dis.* **2017**, *12*, 2101–2109. [[CrossRef](#)] [[PubMed](#)]
117. Xu, Y.; Yamashiro, T.; Moriya, H.; Tsubakimoto, M.; Tsuchiya, N.; Nagatani, Y.; Matsuoka, S.; Murayama, S. Hyperinflated lungs compress the heart during expiration in COPD patients: A new finding on dynamic-ventilation computed tomography. *Int. J. Chronic Obstr. Pulm. Dis.* **2017**, *12*, 3123–3131. [[CrossRef](#)]
118. Hashimoto, M.; Nagatani, Y.; Oshio, Y.; Nitta, N.; Yamashiro, T.; Tsukagoshi, S.; Ushio, N.; Mayumi, M.; Kimoto, T.; Igarashi, T.; et al. Preoperative assessment of pleural adhesion by Four-Dimensional Ultra-Low-Dose Computed Tomography (4D-ULDCT) with Adaptive Iterative Dose Reduction using Three-Dimensional processing (AIDR-3D). *Eur. J. Radiol.* **2018**, *98*, 179–186. [[CrossRef](#)]
119. Xu, Y.; Yamashiro, T.; Moriya, H.; Tsubakimoto, M.; Nagatani, Y.; Matsuoka, S.; Murayama, S. Strain measurement on four-dimensional dynamic-ventilation CT: Quantitative analysis of abnormal respiratory deformation of the lung in COPD. *Int. J. Chronic Obstr. Pulm. Dis.* **2018**, *14*, 65–72. [[CrossRef](#)] [[PubMed](#)]
120. Yamashiro, T.; for the ACTive Study Group investigators; Moriya, H.; Tsubakimoto, M.; Nagatani, Y.; Kimoto, T.; Murayama, S. Preoperative assessment of parietal pleural invasion/adhesion of subpleural lung cancer: Advantage of software-assisted analysis of 4-dimensional dynamic-ventilation computed tomography. *Eur. Radiol.* **2019**, *29*, 5247–5252. [[CrossRef](#)]
121. Nagatani, Y.; Yoshigoe, M.; Tsukagoshi, S.; Ushio, N.; Ohashi, K.; Nitta, N.; Kimoto, T.; Uranishi, A.; Sato, S.; Mayumi, M.; et al. Peripheral bronchial luminal conspicuity on dynamic-ventilation computed tomography: Association with radiation doses and temporal resolution by using an ex vivo porcine lung phantom. *Acta Radiol.* **2020**, *61*, 1608–1617. [[CrossRef](#)]

122. Nagatani, Y.; Hashimoto, M.; Oshio, Y.; Sato, S.; Hanaoka, J.; Fukunaga, K.; Uemura, R.; Yoshigoe, M.; Nitta, N.; Usio, N.; et al. Preoperative assessment of localized pleural adhesion: Utility of software-assisted analysis on dynamic-ventilation computed tomography. *Eur. J. Radiol.* **2020**, *133*, 109347. [[CrossRef](#)] [[PubMed](#)]
123. Sato, S.; Nagatani, Y.; Hashimoto, M.; Nitta, N.; Hanaoka, J.; Ushio, N.; Tsukagoshi, S.; Uranishi, A.; Kimoto, T.; Oshio, Y.; et al. Usability of the lateral decubitus position on four-dimensional ultra-low-dose computed tomography for the detection of localized pleural adhesion in the pulmonary apical region. *Acta Radiol.* **2021**, *62*, 462–473. [[CrossRef](#)] [[PubMed](#)]

**Disclaimer/Publisher's Note:** The statements, opinions and data contained in all publications are solely those of the individual author(s) and contributor(s) and not of MDPI and/or the editor(s). MDPI and/or the editor(s) disclaim responsibility for any injury to people or property resulting from any ideas, methods, instructions or products referred to in the content.